LeBlanc, D.E., et al., 2023, Laurentide Ice Sheet persistence during Pleistocene interglacials: Geology, https://doi.org/10.1130/G50820.1

Supplemental Material for
Laurentide Ice Sheet persistence across Pleistocene interglacials

Danielle E. LeBlanc[1]*; Jeremy D. Shakun[1]; Lee B. Corbett[2]; Paul R. Bierman[2]; Marc W. Caffee[3]; and Alan J. Hidy[4]

[1] Department of Earth and Environmental Sciences, Boston College, Chestnut Hill, MA, USA
[2] Rubenstein School of the Environment and Natural Resources, University of Vermont, Burlington, VT, USA
[3] Department of Physics and Astronomy and Department of Earth, Atmospheric, and Planetary Sciences, Purdue University, West Lafayette, IN, USA
[4] Lawrence Livermore National Laboratory, Livermore, CA

Sediment provenance

The geochemistry and lithology of ocean sediments in both the coarse and fine fraction aids in identifying their source. In the North Atlantic, provenance tracing is complicated by the similar geologic history of the surrounding continents (Hoffman, 1988), yet some work has demonstrated that the different positioning of geologic terranes and the unique mixtures of rock types may manifest as a diagnostic signal capable of linking marine sediments to their source area(s) (Hemming et al., 2000; Hemming, 2004). Previous provenance work on the coarse fractions in or nearby cores used in this study provides strong evidence for a northeastern Canadian source for H1, H2, H3, H4, H5, and H6 on the western side of the basin as well as for H1, H2, H4, and H5 in the east (Hemming, 2004). These layers contain pronounced increases in detrital carbonate, which is perhaps the most diagnostic feature of Heinrich layers (Bond et al., 1992; Broecker et al., 1992; Hemming, 2004) and has been linked to Paleozoic basins in and near Hudson Strait using biomarker fingerprinting and sedimentation patterns (Andrews and Tedesco, 1992; Hemming, 2004; Naafs et al., 2013). H1, H2, H3, and H4 from the northwest Atlantic near Orphan Knoll (V23-14 and EW9303-GGC31), which are close to the western sites used in this study, also possess predominantly Paleoproterozoic-age grains and a smaller component of older and younger grains, which is characteristic of a Hudson Strait source (Gwiazda et al., 1996a; Hemming et al., 2000; Hemming and Hajdas, 2003; Downing and Hemming, 2012; Downing et al., 2013). Paleoproterozoic terranes can be found across Baffin Island as well as to its west and south (e.g. see Figure 1 from Downing et al., 2013). Conversely, ambient IRD between Heinrich layers from Orphan Knoll contains abundant Appalachian- and Grenville-age grains, suggesting a wider range of sources, including the southeastern LIS region (Hemming et al., 2000; Downing and Hemming, 2012). The predominantly Paleoproterozoic ages of grains across last glacial sediments and smaller components of younger and older grains suggest sediment sources came from a broad area but most likely were focused to the northwest and east of Hudson Bay. In eastern North Atlantic cores, H1, H2, H4, and H5 contain predominantly Canadian-derived IRD (Gwiazda et al., 1996a; Hemming et al., 1998) while Pb isotope data show that H3 more closely resembles ambient sediments, which are linked to a Greenland and/or a Scandinavian origin (Gwiazda et al., 1996b; Hemming et al., 1998; Snoeckx et al., 1999).

Sediment processing

We obtained a total of 456 sediment samples (10 cm^3 each) from six North Atlantic sediment cores, three on the eastern side of the basin (IODP U1308 (49.8°N, 24.2°W, 3900 m), DSDP609 (49.9°N, 24.2°W, 3427 m), and BOFS-5K (50.7°N, 21.9°W, 3547)) and three on the western side (IODP U1302 (50.2°N, 45.6°W, 3560 m), IODP U1303 (50.2°N, 45.7°W, 3520 m), and EW93-02 JPC02 (48.8°N, 45.1°W, 1251 m)). The number of samples used for each Heinrich and non-Heinrich interval varied. From western sites, 22 ± 6 and 11 ± 3 samples (mean and standard deviation) were collected from each background and Heinrich layer, respectively, while 25 ± 6 and 10 ± 2 samples were collected from these intervals at eastern sites (Fig. S3-7). Samples were soaked in a light deflocculant solution of sodium metaphosphate and sieved to isolate the >63 um size fraction. Each sample was then rinsed in a 10 % HCl solution to remove carbonates. These samples were next amalgamated within Heinrich and background layers across east and west sites, producing a total of 13 samples from each side of the basin. Heinrich intervals were identified using a variety of tracers from previous work, including Ca/Sr, detrital carbonate and lithic concentrations, bulk $\delta^{18}O$, and magnetic susceptibility (Broecker et al., 1992; Manighetti et al., 1995; Robinson et al., 1995; Stoner et al., 1996; Rosell-Mele et al., 1997; Rasmussen et al., 2003; Channell et al., 2012) (Fig. S3-7). Weakly magnetized minerals were removed via magnetic separation. Lastly, quartz was isolated through two 24-hour heated 50% HCl etches followed by repeated etches in a weak (0.125 to 0.25%) HF/HNO_3 solution. ICP-OES analysis of quartz aliquots was used to estimate sample impurities and native ^{27}Al. Samples with high impurities were re-etched until low Al concentrations (<150 ppm) were obtained.

Sample grain size

While the definition of IRD size fraction varies widely across the literature (e.g. McKay et al., 2022), we use the >63 um fraction to ensure enough material for measurement. Although the highest bottom current speeds could transport grains >63 μm in some areas (McCave and Andrews, 2019), this size fraction is generally thought to be safe from resuspension, and we target locations where resuspension is unlikely.

U1302/03 (water depth: 3560 m and 3520 m) are located on a flank of Orphan Knoll above surrounding canyons, protecting this site from input of non-iceberg-rafted sands (e.g. turbidity currents) (Channell et al., 2012). EW93-02 JPC-02 (water depth: 1251 m) is near U1302/03 in the path of LIS icebergs and under the influence of Labrador Sea Water but above stronger Western Boundary Undercurrents, reducing the likelihood of non-IRD input in the >63 um size fraction (Hillaire-Marcel et al., 1994; Rasmussen et al., 2003). Site 609/ U1308 (water depth: 3427 m) sits within North Atlantic Deep Water but out of the path of any overflows from the Norwegian-Greenland Sea (Hodell et al., 2008), suggesting the >63 um fraction is solely from icebergs. BOFS-5K (water depth: 3547 m) is in a similar oceanographic location to Site 609/U1308 on the East Thulean Rise in the central North Atlantic.

Cosmogenic nuclide extraction

Purified Be and Al were extracted from quartz at the University of Vermont National Science Foundation Community Cosmogenic Facility using the methods outlined in Corbett et al. (2016). Samples were prepared in three batches, each containing 8-10 samples and 2-4 process blanks. We added ~0.84 g of in-house made 291 μg/mL ^9Be beryl carrier to each sample (totaling ~240 μg ^9Be), and ^{27}Al carrier (SPEX ICP standard, 1000 ppm) was added if samples contained <1500 μg of native Al. The total ^{27}Al (quantified using ICP-OES, measured in replicate using a Yittrum internal standard) in each sample averaged 2236 ± 372 μg. $^{10}Be/^9Be$

ratios were measured at the Lawrence Livermore National Laboratory Center for Accelerator Mass Spectrometry and normalized to primary standard 07KNSTD3110 with an assumed ratio of 2.850 x 10^{-12} [69] (Table S1). $^{26}Al/^{27}Al$ ratios were measured at the Purdue Rare Isotope Measurement Laboratory and normalized to KNSTD with an assumed ratio of 1.818 x 10^{-12} [70] (Table S3).

Blanks

Twelve (^{10}Be) and ten (^{26}Al) procedural blanks were processed alongside samples during nuclide extraction and measured to estimate background nuclides associated with laboratory processing and accelerator mass spectrometry analysis. We corrected measured sample $^{10}Be/^{9}Be$ and $^{26}Al/^{27}Al$ ratios for this contribution by subtracting the mean of all the blanks (1.03 ± 0.53 x 10^{-15} and 7.91 ± 0.26 x 10^{-16}, respectively). We quantified the blank uncertainty as the standard error of the mean and combined it with the measurement uncertainty of the sample nuclide abundances in quadrature (Tables S2 and S4).

Decay correction

Nuclide concentrations were corrected for radioactive decay on the seafloor to the time of deposition (Table S5). We used ages for Heinrich layers from Hemming (2004), and midpoints between these ages for background layers. Decay correction increases measured $^{26}Al/^{10}Be$ ratios by 1-3%.

Interpretive modeling

To aid interpretation of the data, a simple 1-D model is used to simulate ice cover based on three exposure scenarios: (1) a frequent-interglacial scenario, with exposure during every Pleistocene interglacial in the LR04 $\delta^{18}O$ stack, (2) a skipped-interglacial scenario, which follows the frequent-interglacial scenario until 1 Ma but then only simulates exposure at MIS 5e, 9, and 11, and (3) a lengthened early Pleistocene interglacial scenario, similar to the skipped-interglacial scenario except that exposure periods prior to 1 Ma are twice as long as those after 1 Ma. We assess results for interglacial lengths of 1 and 10 kyr.

Results from these simulations support our conclusion that there were not extended ice-free intervals across most interglacials of the past million years in sediment source regions. For instance, if there were exposure during every Pleistocene interglacial, it could only have been on the order of 1-2 kyr, otherwise $^{26}Al/^{10}Be$ ratios would be higher than in most of our samples (Fig. S1 and S2, scenario 1). This result holds when limiting exposure to the few especially strong interglacials during the past million years (i.e., MIS 5e, 9, and 11) (Fig. S1 and S2, scenario 2). Simulated $^{26}Al/^{10}Be$ ratios could overlap with more of our data for longer exposures (~5-10 kyr) during these few mid-to-late Pleistocene interglacials, but only if there was greater early Pleistocene exposure and much of the sediment came from very slowly eroding areas where old nuclides are preserved (Fig. S1 and S2, scenario 3). However, ^{10}Be concentrations would be much higher than our sample values in this case.

The model calculates ^{10}Be and ^{26}Al evolution in a bedrock column at 1 kyr time steps for various exposure and erosion scenarios over the past 8 Myr (5 Myr of exposure to initialize conditions + 3 Myr of Pleistocene ice cover change). For each model run, nuclide production is simulated during intervals of exposure, while nuclide production ceases and erosion occurs during intervals of ice cover. We assume sea-level, high-latitude production rates, including production by muons, calculated using the MATLAB implementation in Balco et al., (2008) of

the method of Heisinger et al. (2002) and a $^{26}Al/^{10}Be$ surface production ratio of 7.3 (Corbett et al., 2017). Nuclides decay continuously throughout model runs. To incorporate erosion, the "top" of the bedrock column is redefined as the eroded depth at each time step. For instance, an erosion rate of 10 mm/kyr would remove the upper 10 mm of bedrock over one timestep, and the following timestep would start with the concentration at 10 mm depth as the new surface. The model uses the following equation to calculate concentrations in the bedrock column:

$$N(t,z) = N(t-1,z) \cdot e^{\frac{((-\Delta t \ln 2)/t_1)}{2}} + P(z) \cdot \Delta t \, (1 - C_{ice})$$

Where N(t, z) is the nuclide (^{10}Be or ^{26}Al) concentration, which changes with both depth (z) and time (t), N(t-1, z) is the nuclide concentration as a function of the previous time step (t-1) and depth, Δt is the time step length (1 kyr), $t_{1/2}$ is the nuclide half-life, P(z) is the nuclide production rate as a function of depth, and C_{ice} is 1 during ice cover and 0 during exposure. Prior to 3 Ma, constant production of both nuclides and erosion at 20 mm/kyr occurs. We run each exposure scenario over a range of erosion rates (1, 10, and 100 mm/kyr) to assess the sensitivity of simulated ^{10}Be and ^{26}Al concentrations to erosion.

To explore the potential impact of nonstationary erosion rates, we rerun exposure scenario 1 from above through three additional simulations with accelerating erosion over the Pleistocene of different baselines and magnitudes of acceleration (Fig. S8). These simulations suggest 10-kyr exposure events every interglacial could yield $^{26}Al/^{10}Be$ ratios as low as we measured, but only if erosion rates accelerated one to two orders of magnitude over the Pleistocene. We are unaware of long-term erosion rate reconstructions for the LIS, but a recent reconstruction for Eurasian ice sheets suggests erosion rate changes were much smaller and in fact decreased from the mid to late Pleistocene (Lien et al., 2022). Furthermore, simulated ^{10}Be concentrations in these accelerating erosion simulations are an order of magnitude lower than the concentrations we measured in IRD. We therefore consider accelerating erosion an unlikely explanation for the low $^{26}Al/^{10}Be$ ratios we measured, and favor quasi-persistent ice cover over the past million years as the most parsimonious interpretation of the dataset.

To assess whether nuclide production through thin ice cover during glacials might yield low $^{26}Al/^{10}Be$ ratios despite frequent 10-kyr interglacial exposures, we rerun scenario 1 from above but simulate nuclide production by muons through 50 m of ice when covered (Fig. S9). Simulated $^{26}Al/^{10}Be$ ratios are higher than in our default simulation with no production through ice, discounting this explanation. The MATLAB code used for forward model simulations is available at https://github.com/danielleeleblanc/LeBlanc-et-al-2022-Unpublished.

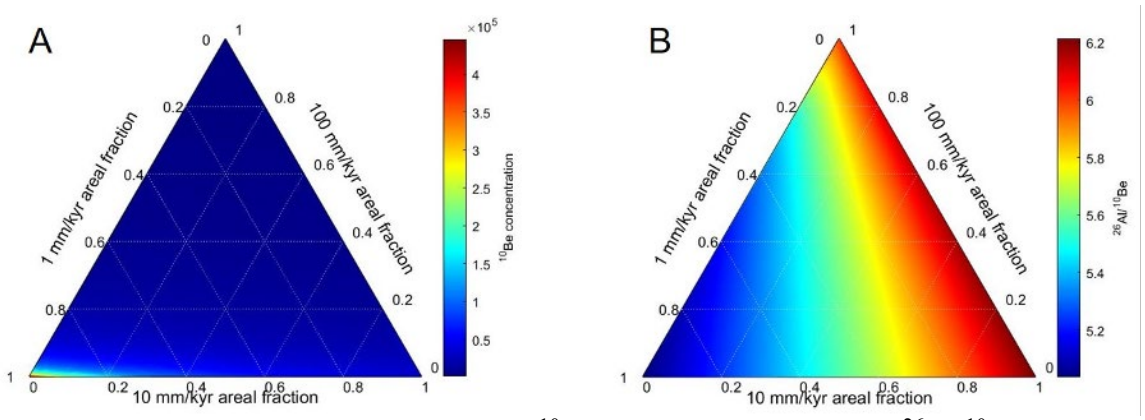

Fig. S1. The ternary diagrams show how (A) ^{10}Be concentrations and (B) ^{26}Al/^{10}Be ratios mix between three end members as a function of the areal fraction of sediment source areas each occupies. End members are simulated values from Fig. 3 using benthic δ^{18}O threshold of 3.7 ‰ for 1, 10, and 100 mm/kyr glacial erosion rates. See Bierman et al., 2016 for mixing equations.

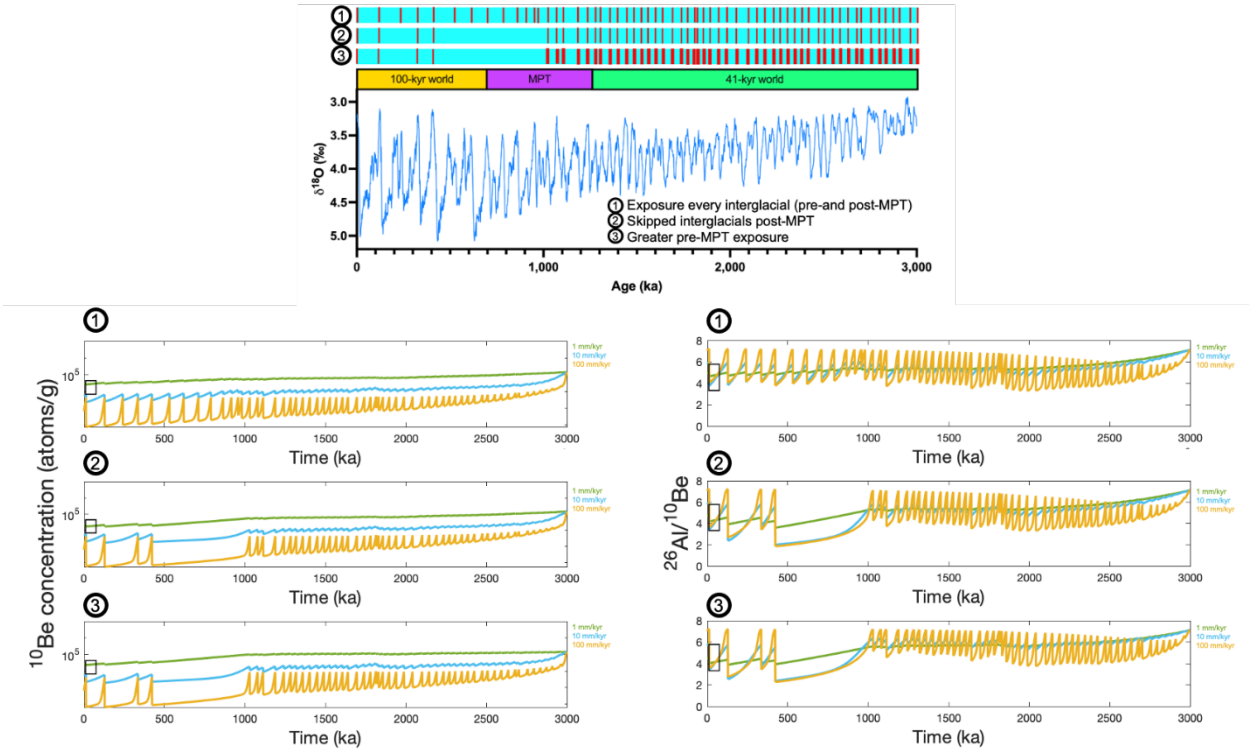

Fig. S2. Modeled cosmogenic nuclides for 1-kyr interglacial exposures. Simulated ^{10}Be concentrations (left) and ^{26}Al/^{10}Be ratios (right) over the past 3 Myr for three ice cover scenarios (top) for 1-kyr interglacial exposures using three different erosion rates: 1, 10, and 100 mm/kyr. Scenario 1 has exposure during every Pleistocene interglacial. Scenario 2 features exposure during every interglacial until 1 Ma, but only during select interglacials thereafter (MIS 1, 5e, 9, and 11). Scenario 3 is the same as scenario 2 but interglacial exposures are twice as long before 1 Ma as after (i.e., scenarios with 1-kyr exposure after 1 Ma have 2-kyr exposure before 1 Ma). The LR04 benthic oxygen isotope stack is shown (top) as a proxy for global ice volume[38]. The mid-Pleistocene transition (MPT) marks the shift from 41-kyr to ~100-kyr glacial cycles. Boxes from 64-14 ka in lower panels show the range of our measured values.

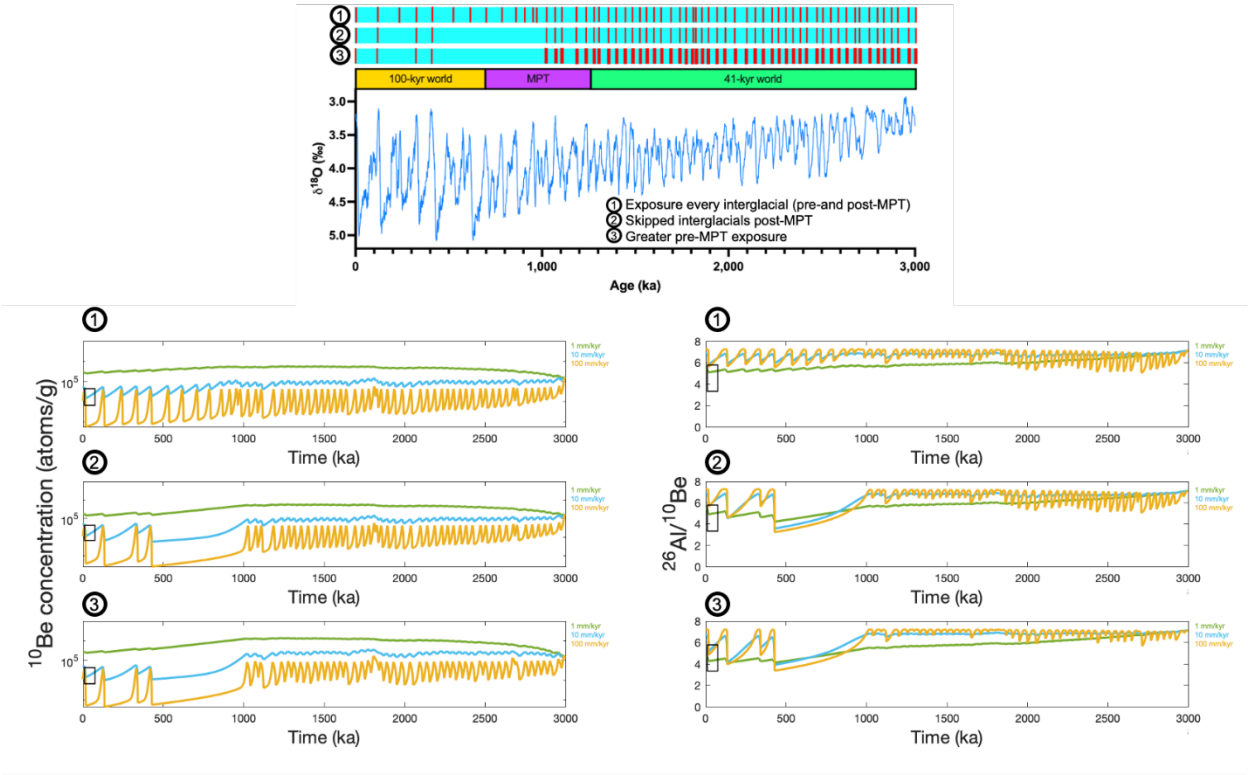

Fig. S3. Modeled cosmogenic nuclides for 10-kyr interglacial exposures. The same as Fig. S1 but with 10-kyr interglacial exposures.

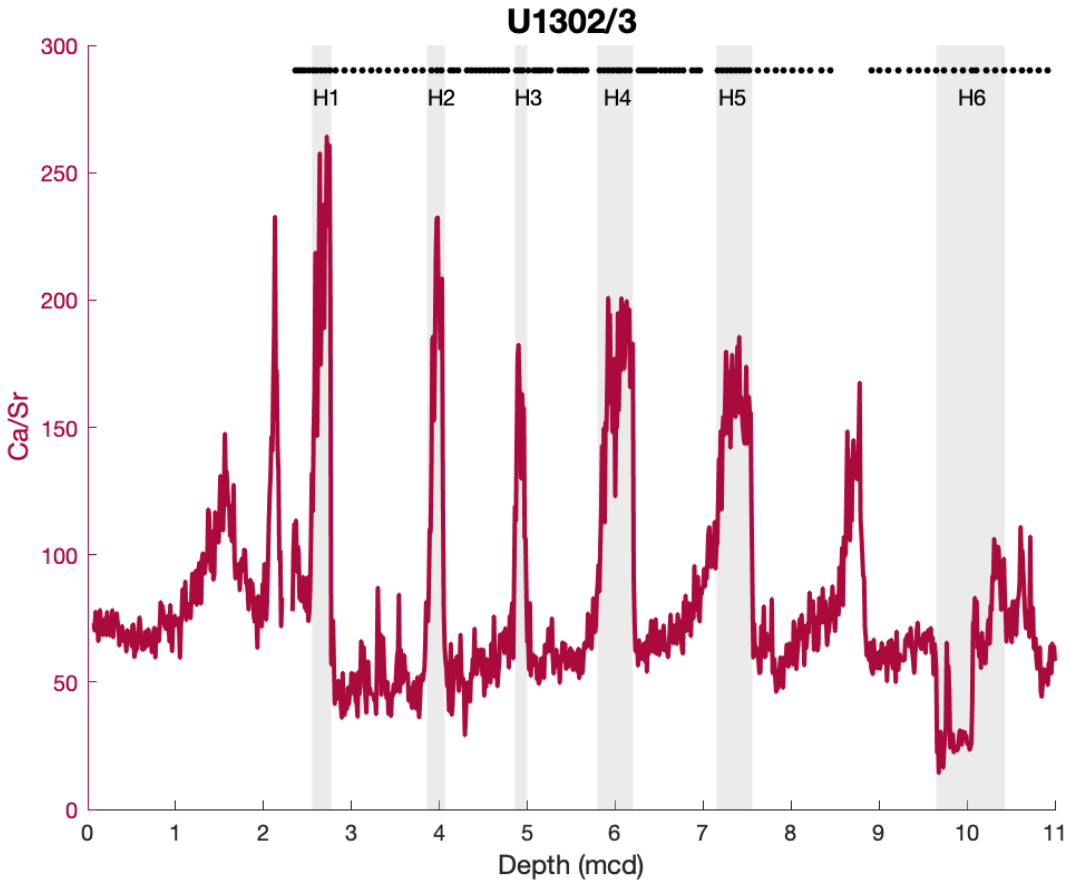

Fig. S4. Identification of Heinrich layers in U1302/3. Peaks in Ca/Sr reflect detrital carbonate-rich Heinrich layers (Channell et al., 2012; Channell and Hodell, 2013). Black dots at the top indicate the locations of our samples.

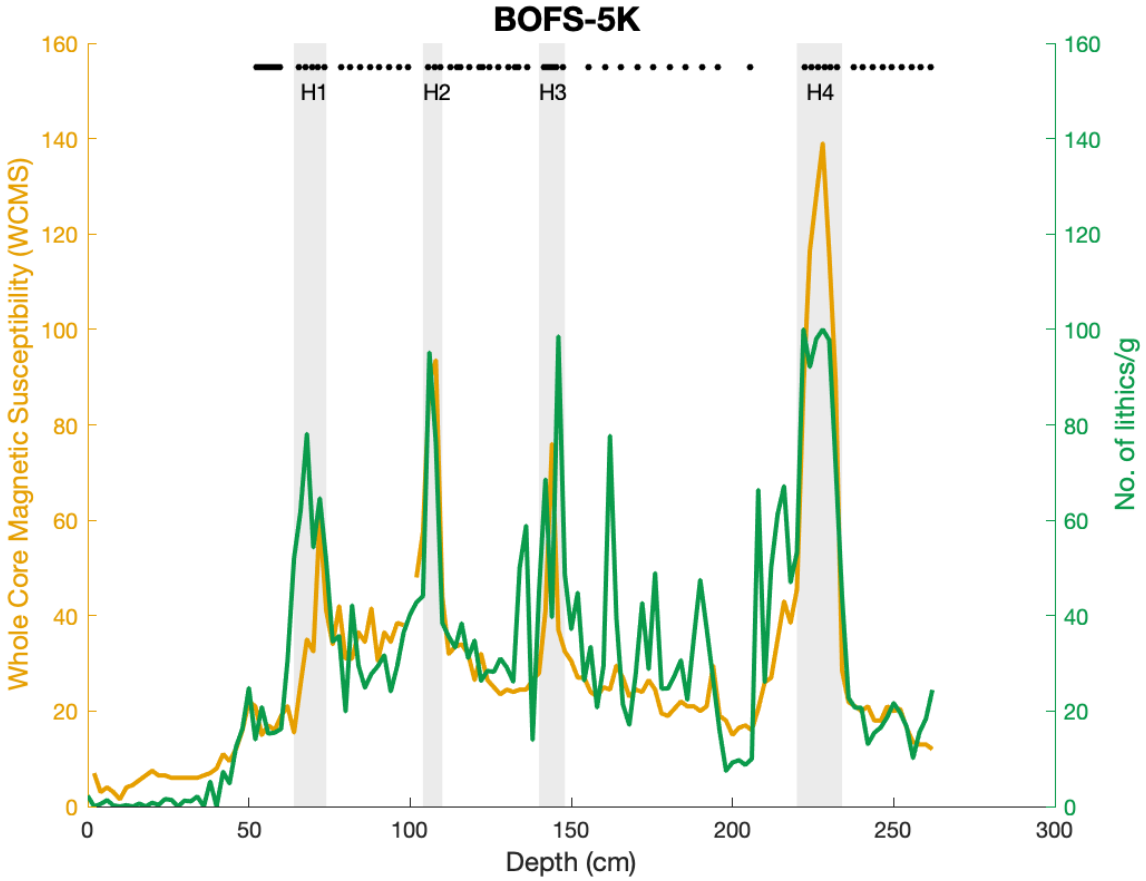

Fig. S5. Identification of Heinrich layers in BOFS-5K. Peaks in magnetic susceptibility (yellow) and lithics concentration (green) reflect IRD-rich Heinrich layers (Manighetti et al., 1995; Robinson et al., 1995; Rosell-Mele et al., 1997). Black dots at the top indicate the locations of our samples.

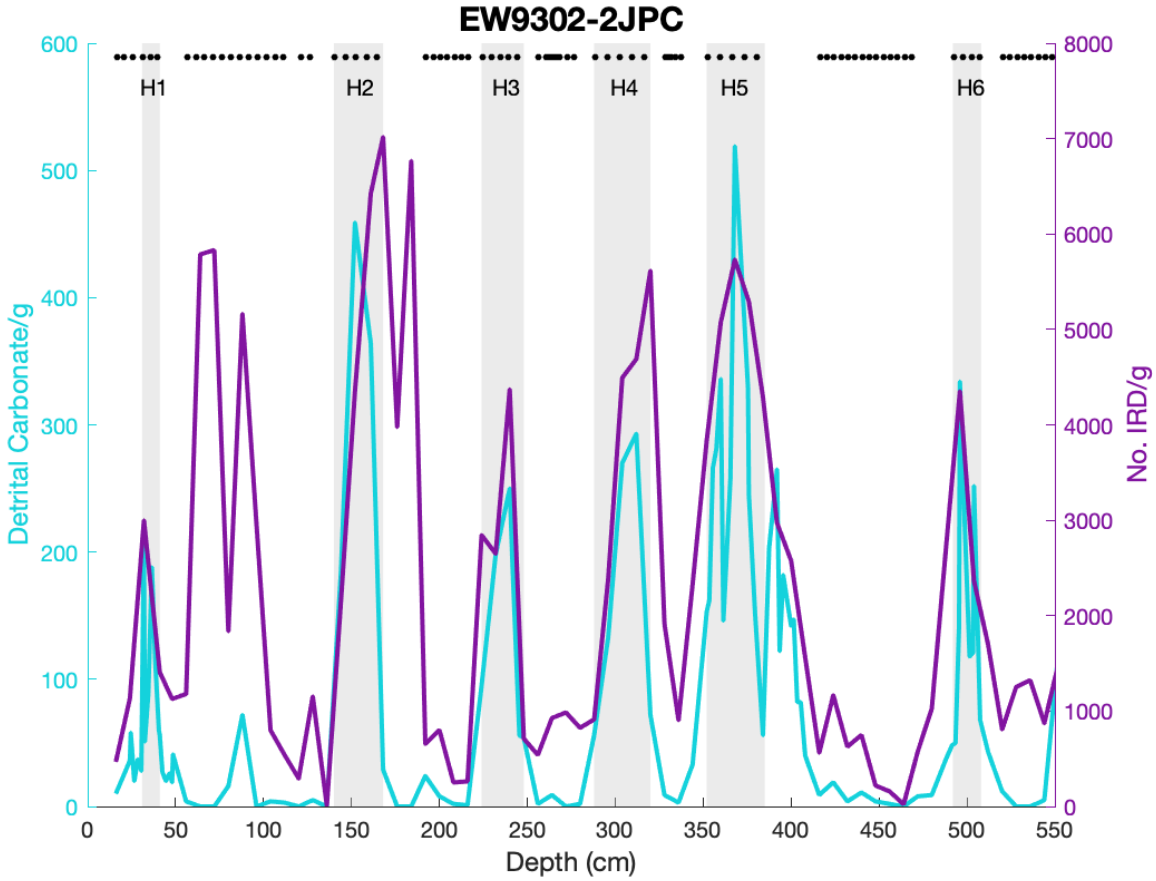

Fig. S6. Identification of Heinrich layers in EW9302-2JPC. Peaks in detrital carbonate (blue) and IRD concentration (purple) reflect Heinrich layers (Rasmussen et al., 2003; Marcott et al., 2011). Black dots at the top indicate the locations of our samples.

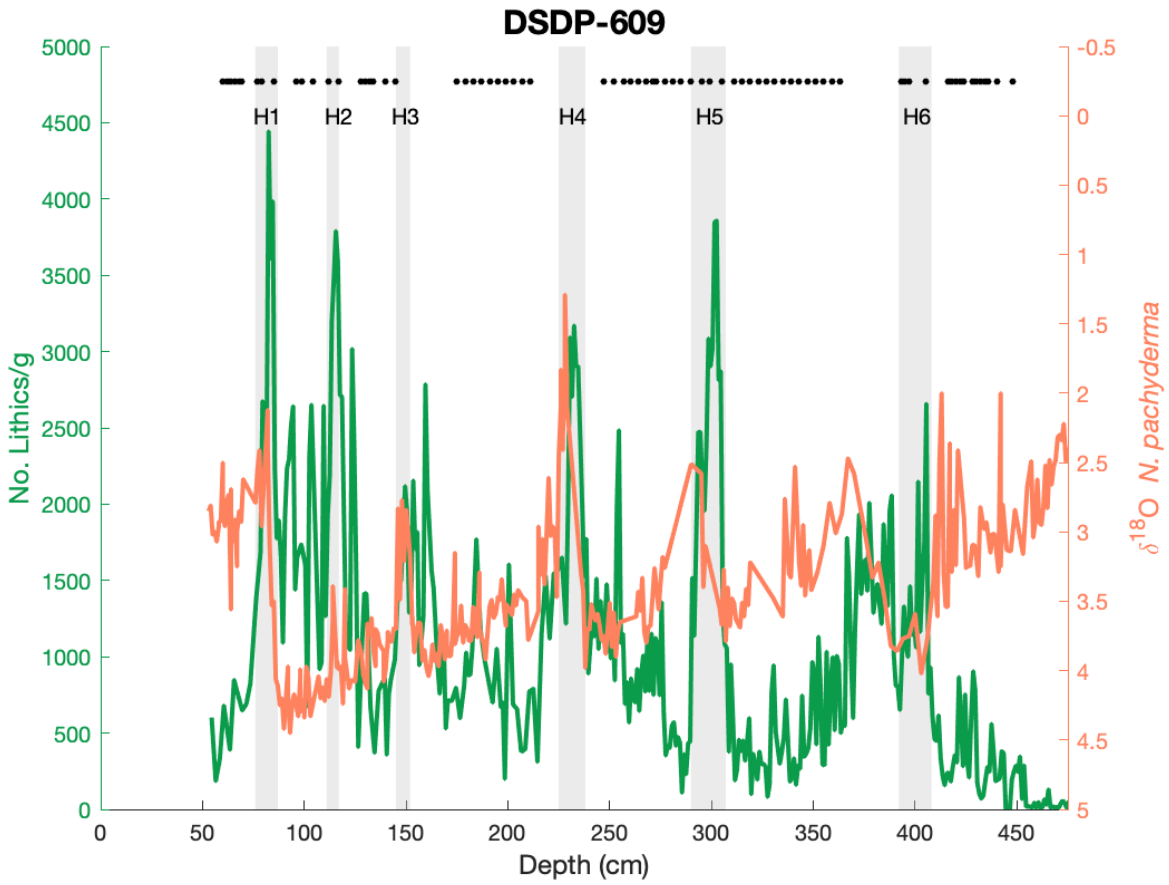

Fig. S7. Identification of Heinrich layers in DSDP-609. Peaks in lithics concentration (green) and *N. pachyderma (s.)* $\delta^{18}O$ (peach) depletions reflect IRD and freshwater pulses associated with Heinrich events (Broecker et al., 1992). Black dots at the top indicate the locations of our samples.

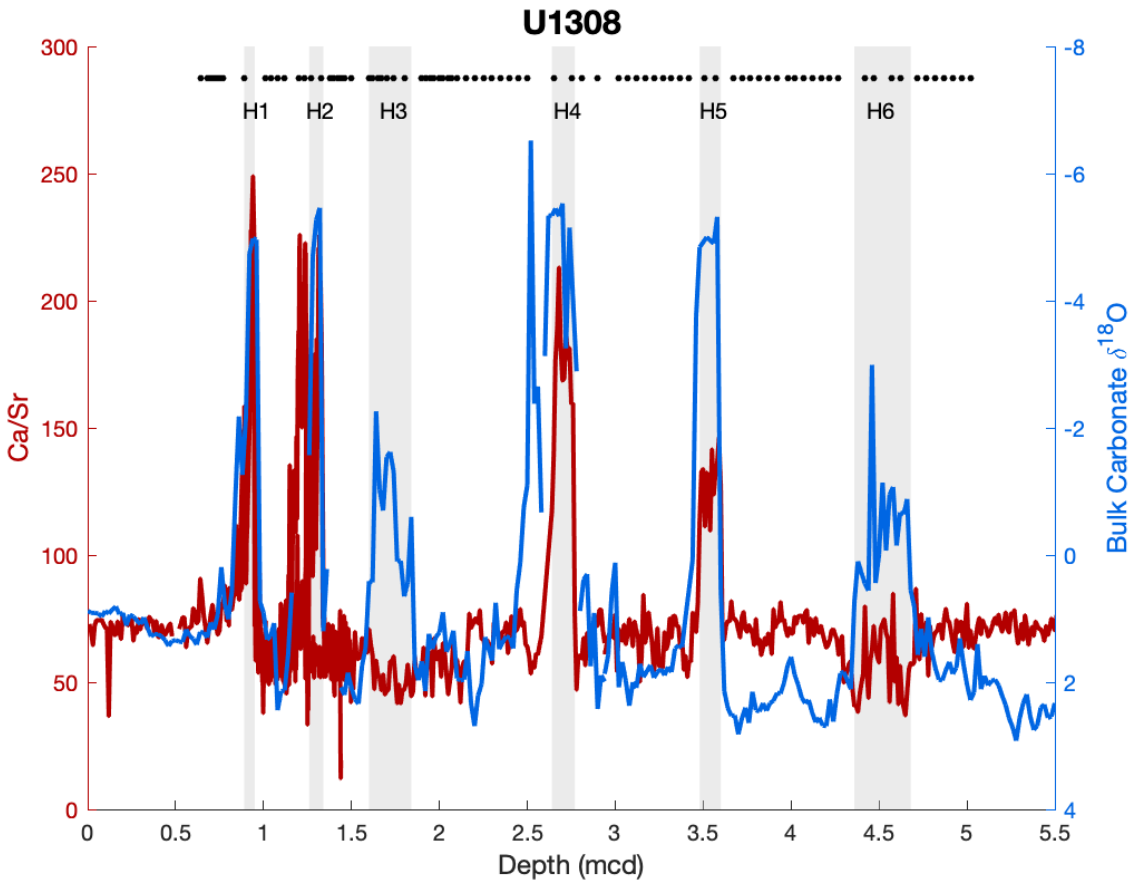

Fig. S8. Identification of Heinrich layers in U1308. Ca/Sr (red) peaks and bulk carbonate $\delta^{18}O$ (blue) depletions reflect detrital carbonate-rich Heinrich layers (Hodell et al., 2017). Black dots at the top indicate the locations of our samples.

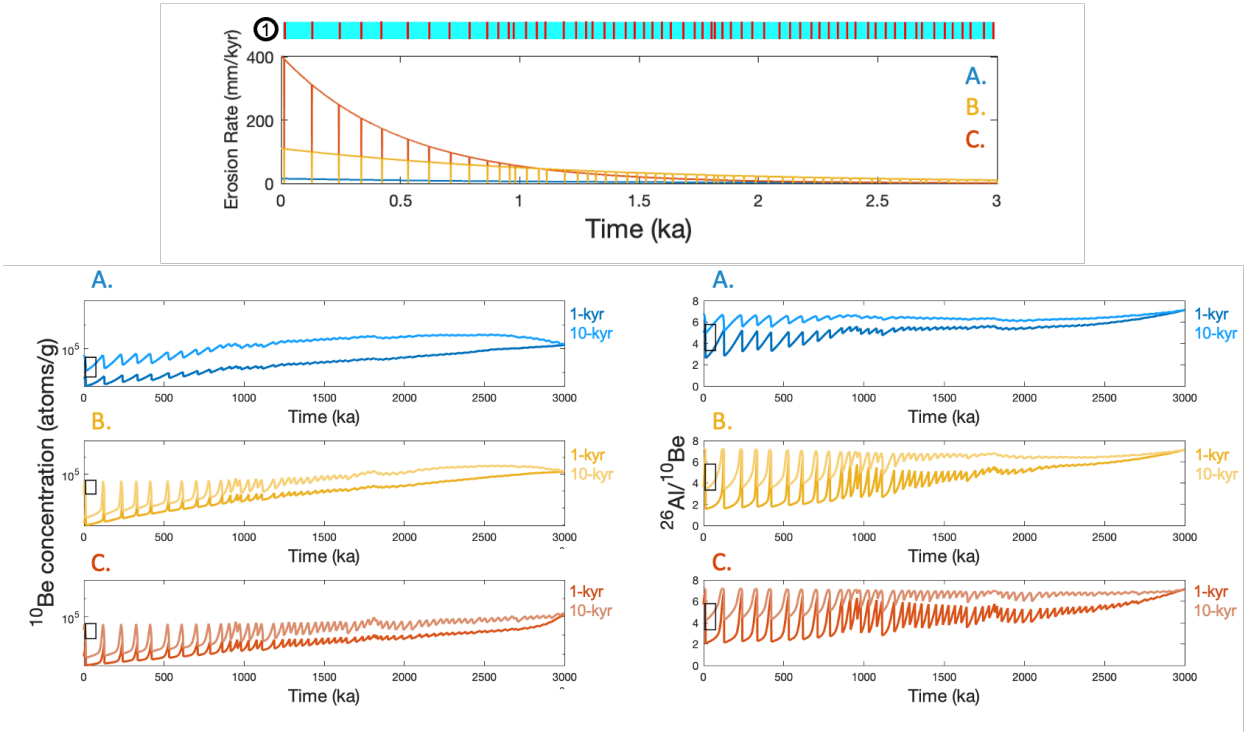

Fig. S9. Modeled cosmogenic nuclides for 1-and 10-kyr interglacial exposures with accelerating erosion. Simulated ^{10}Be concentrations (left) and ^{26}Al/^{10}Be ratios (right) over the past 3 Myr for ice cover scenario 1 shown at the top (same as in Fig. S1) with 1- and 10-kyr interglacial exposure using three different accelerating erosion scenarios (A, B, and C on top plot). Boxes from 65-14 ka show the range of our measured values. While erosion scenarios B and C yield ^{26}Al/^{10}Be ratios as low as measured, we consider these scenarios unlikely because they imply subglacial erosion was negligible in the early Pleistocene and then increased orders of magnitude in the late Pleistocene.

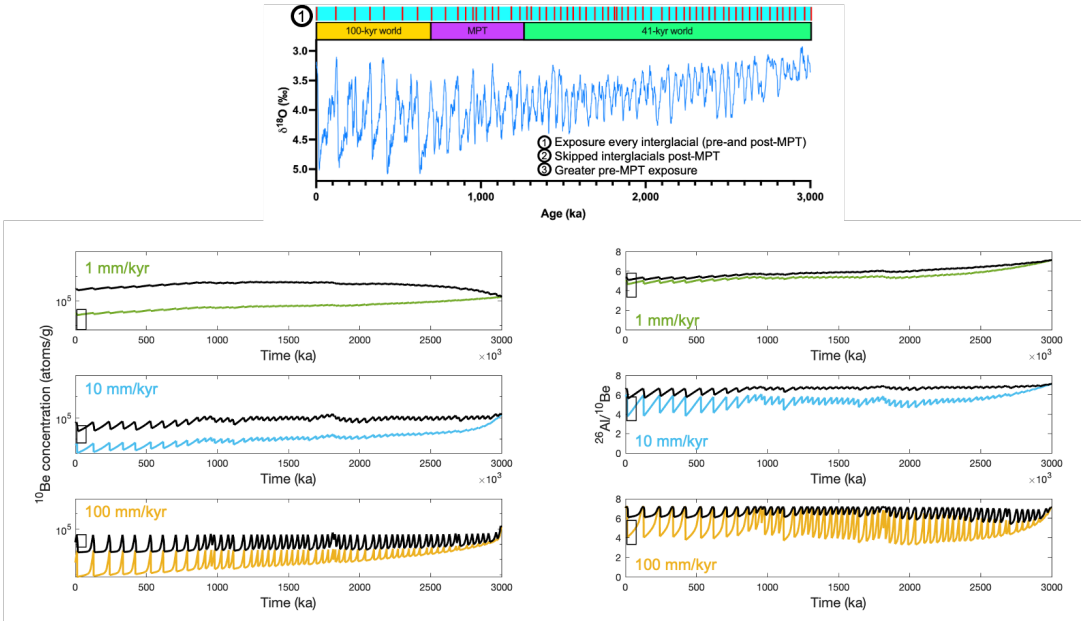

Fig. S10. The same as in Fig. S2 for ice cover scenario 1 (colored lines), but also showing results including production by muons through 50 m of ice during glacials (black).

Sample Name	Quartz Mass (g)	Mass of ^{9}Be Added (µg)*	AMS Cathode Number	Uncorrected ^{10}Be/^{9}Be Ratio**	Uncorrected ^{10}Be/^{9}Be Ratio Uncertainty**	Background-Corrected ^{10}Be/^{9}Be Ratio	Background-Corrected ^{10}Be/^{9}Be Ratio 1σ Uncertainty	^{10}Be Concentration (atoms g^{-1})	^{10}Be Concentration 1σ Uncertainty (atoms g^{-1})	
EB0	4.1419	243.2	BE48152	6.784E-15	4.375E-16	5.903E-15	5.746E-16	2.316E+04	2.255E+03	Batch 3
EB2	4.9050	243.1	BE48153	9.555E-15	4.931E-16	8.674E-15	6.180E-16	2.872E+04	2.046E+03	
EH3	4.2999	242.9	BE48154	1.017E-14	6.273E-16	9.287E-15	7.296E-16	3.505E+04	2.754E+03	
EH6	4.7744	242.1	BE48155	1.068E-14	6.484E-16	9.797E-15	7.478E-16	3.320E+04	2.534E+03	
EB6	4.9062	242.2	BE48158	1.196E-14	4.996E-16	1.108E-14	6.232E-16	3.655E+04	2.056E+03	
WB0	5.8679	242.7	BE48159	3.607E-15	3.528E-16	2.726E-15	5.131E-16	7.536E+03	1.418E+03	
WB3	5.9715	242.8	BE48160	5.959E-15	4.463E-16	5.079E-15	5.814E-16	1.380E+04	1.580E+03	
WB4	4.4646	241.9	BE48161	5.290E-15	5.067E-16	4.409E-15	6.290E-16	1.597E+04	2.278E+03	
EB3	13.5617	240.8	BE47420	3.779E-14	9.659E-16	3.632E-14	1.172E-15	4.310E+04	1.390E+03	Batch 2
EB4	13.6682	241.8	BE47422	3.777E-14	1.134E-15	3.630E-14	1.314E-15	4.292E+04	1.553E+03	
EB5	4.9141	242.0	BE47423	9.790E-15	9.795E-16	8.323E-15	1.183E-15	2.739E+04	3.893E+03	
WB2	4.1814	240.3	BE47425	4.140E-15	3.121E-16	2.673E-15	7.331E-16	1.027E+04	2.816E+03	
WB5	4.3290	241.6	BE47426	6.240E-15	4.722E-16	4.774E-15	8.143E-16	1.780E+04	3.037E+03	
WB6	9.4252	241.9	BE47428	1.019E-14	7.778E-16	8.727E-15	1.022E-15	1.497E+04	1.753E+03	
WH3	6.7512	241.5	BE47429	5.513E-15	4.942E-16	4.047E-15	8.272E-16	9.674E+03	1.978E+03	
WH6	8.1019	240.4	BE47431	8.867E-15	4.990E-16	7.400E-15	8.301E-16	1.468E+04	1.646E+03	
EH1	8.2163	242.7	BE47239	5.831E-15	5.612E-16	5.092E-15	6.119E-16	1.005E+04	1.208E+03	Batch 1
WH1	8.7254	242.2	BE47240	4.622E-15	5.207E-16	3.883E-15	5.750E-16	7.201E+03	1.066E+03	
EB1	6.8760	242.5	BE47242	9.713E-15	5.985E-16	8.974E-15	6.463E-16	2.115E+04	1.523E+03	
WB1	9.4924	241.7	BE47243	5.466E-15	4.418E-16	4.727E-15	5.046E-16	8.042E+03	8.585E+02	
EH2	9.0450	241.4	BE47244	6.727E-15	4.343E-16	5.988E-15	4.981E-16	1.068E+04	8.882E+02	
WH2	6.0834	242.4	BE47245	3.815E-15	3.468E-16	3.076E-15	4.240E-16	8.191E+03	1.129E+03	
EH4	12.0356	242.2	BE47246	1.177E-14	5.489E-16	1.103E-14	6.006E-16	1.484E+04	8.078E+02	
WH4	12.9206	242.7	BE47247	9.624E-15	5.729E-16	8.885E-15	6.226E-16	1.115E+04	7.814E+02	
EH5	7.2881	241.0	BE47249	7.123E-15	3.967E-16	6.384E-15	4.657E-16	1.411E+04	1.029E+03	
WH5	14.5706	241.3	BE47250	1.229E-14	7.775E-16	1.155E-14	8.148E-16	1.278E+04	9.017E+02	

*^{9}Be was added through a beryl carrier made at University of Vermont with a concentration of 291 µg mL^{-1}.

**Isotopic analysis was conducted at Lawrence Livermore National Laboratory; ratios were normalized against standard 07KNSTD3110 with an assumed ratio of 2850 x 10^{-15} [69].

Table S1. ^{10}Be measurements in North Atlantic ice-rafted debris. All western and eastern Heinrich layers are indicated by 'WH' and 'EH', respectively. Each number refers to the corresponding Heinrich interval. Intervening background intervals are labelled as 'WB' and 'EB' for west and east sides of the North Atlantic, respectively. Numbers for intervening layers start at 0, indicating samples before H1, and increase going down hole. Samples were processed in three batches (shown on right).

Blank Name	UVM Batch Number	Cathode Number	Be Analysis Date	From AMS: $^{10}Be/^{9}Be$ Ratio	From AMS: $^{10}Be/^{9}Be$ Ratio 1σ Uncertainty	
BLK	674	BE48151	2/26/20	1.416E-15	2.363E-16	Batch 3
BLKX	674	BE48156	2/26/20	8.465E-16	1.804E-16	
BLKXX	674	BE48157	2/26/20	6.623E-16	1.562E-16	
BLKXXX	674	BE48162	2/26/20	5.968E-16	1.656E-16	
BLK	669	BE47421	11/20/19	1.293E-15	3.138E-16	Batch 2
BLKX	669	BE47424	11/20/19	2.364E-15	3.451E-16	
BLKXX	669	BE47427	11/20/19	7.706E-16	1.989E-16	
BLKXXX	669	BE47430	11/20/19	1.440E-15	3.069E-16	
BLK	662	BE47241	9/19/19	9.137E-16	1.867E-16	Batch 1
BLKX	662	BE47248	9/19/19	4.429E-16	1.337E-16	
BLK	664	BE47254	9/19/19	9.622E-16	1.853E-16	
BLKX	664	BE47259	9/19/19	6.370E-16	1.425E-16	
			AVERAGE	1.029E-15		
			STDEV	5.3142E-16		

Table S2. ^{10}Be blank values. Blanks were processed in three batches (shown on right).

Sample Name	Quartz Mass (g)	Total ^{27}Al Quantified by ICP-OES (μg)*	AMS Cathode Number	Uncorrected ^{26}Al/^{27}Al Ratio**	Uncorrected ^{26}Al/^{27}Al Ratio Uncertainty**	Background-Corrected ^{26}Al/^{27}Al Ratio	Background-Corrected ^{26}Al/^{27}Al Ratio Uncertainty	^{26}Al Concentration (atoms g^{-1})	^{26}Al Concentration Uncertainty (atoms g^{-1})	
EB0	4.1419	2029	160449	1.168E-14	1.134E-15	1.089E-14	1.164E-15	1.190E+05	1.273E+04	Batch 3
EB2	4.9050	2193	160450	1.690E-14	1.429E-15	1.611E-14	1.453E-15	1.607E+05	1.450E+04	
EH3	4.2999	2009	160451	1.965E-14	1.667E-15	1.886E-14	1.688E-15	1.967E+05	1.760E+04	
EH6	4.7744	2088	160452	1.970E-14	1.611E-15	1.891E-14	1.632E-15	1.846E+05	1.593E+04	
EB6	4.9062	2348	160455	2.004E-14	1.643E-15	1.924E-14	1.664E-15	2.056E+05	1.778E+04	
WB0	5.8679	3416	160456	3.442E-15	7.257E-16	2.651E-15	7.717E-16	3.444E+04	1.003E+04	
WB3	5.9715	2528	160457	6.132E-15	8.844E-16	5.341E-15	9.226E-16	5.046E+04	8.716E+03	
WB4	4.4646	2066	160458	8.232E-15	9.819E-16	7.441E-15	1.016E-15	7.685E+04	1.050E+04	
EB3	13.5617	2137	160436	6.368E-14	4.317E-15	6.289E-14	4.325E-15	2.212E+05	1.521E+04	Batch 2
EB4	13.6682	2079	160438	5.436E-14	2.658E-15	5.357E-14	2.671E-15	1.818E+05	9.067E+03	
EB5	4.9141	1953	160439	1.713E-14	1.510E-15	1.634E-14	1.532E-15	1.449E+05	1.359E+04	
WB2	4.1814	1930	160441	5.693E-15	8.352E-16	4.902E-15	8.755E-16	5.049E+04	9.018E+03	
WB5	4.3290	2151	160442	9.071E-15	1.045E-15	8.280E-15	1.077E-15	9.183E+04	1.194E+04	
WB6	9.4252	2377	160444	1.080E-14	1.089E-15	1.001E-14	1.120E-15	5.633E+04	6.306E+03	
WH3	6.7512	2412	160445	7.287E-15	1.058E-15	6.495E-15	1.091E-15	5.179E+04	8.696E+03	
WH6	8.1019	2261	160447	9.476E-15	1.142E-15	8.684E-15	1.172E-15	5.410E+04	7.299E+03	
EH1	8.2163	1831	160424	1.111E-14	1.310E-15	1.032E-14	1.336E-15	5.134E+04	6.649E+03	Batch 1
WH1	8.7254	2119	160425	4.887E-15	8.539E-16	4.096E-15	8.933E-16	2.220E+04	4.841E+03	
EB1	6.8760	1854	160427	1.792E-14	1.969E-15	1.713E-14	1.987E-15	1.031E+05	1.196E+04	
WB1	9.4924	2466	160428	7.332E-15	9.514E-16	6.540E-15	9.870E-16	3.792E+04	5.722E+03	
EH2	9.0450	2387	160429	7.419E-15	1.377E-15	6.628E-15	1.402E-15	3.903E+04	8.257E+03	
WH2	6.0834	2081	160430	5.859E-15	8.174E-16	5.068E-15	8.585E-16	3.868E+04	6.553E+03	
EH4	12.0356	2827	160431	1.418E-14	1.296E-15	1.338E-14	1.322E-15	7.016E+04	6.930E+03	
WH4	12.9206	2897	160432	1.312E-14	1.374E-15	1.233E-14	1.399E-15	6.168E+04	6.998E+03	
EH5	7.2881	1682	160434	1.590E-14	1.719E-15	1.510E-14	1.739E-15	7.781E+04	8.958E+03	
WH5	14.5706	2016	160435	2.138E-14	1.563E-15	2.059E-14	1.585E-15	6.357E+04	4.894E+03	
*^{27}Al was added only to samples with insufficient total Al through commercial SPEX ICP standard with a concentration of 1000 μg mL^{-1}. The total here reflects the sum of Al added through carrier and native Al in quartz.										
**Isotopic analysis was conducted at PRIME Laboratory; ratios were normalized against standard KNSTD with an assumed ratio of 1.818 x 10^{-12} [70].										

Table S3. ^{26}Al measurements in North Atlantic ice-rafted debris. All western and eastern Heinrich layers are indicated by 'WH' and 'EH', respectively. Each number refers to the corresponding Heinrich interval. Intervening background intervals are labelled as 'WB' and 'EB' for west and east sides of the North Atlantic, respectively. Numbers for intervening layers start at 0, indicating samples before H1, and increase going down hole. Samples were processed in three batches (shown on right).

Blank Name	UVM Batch Number	Cathode Number	Al Analysis Date	From AMS: $^{26}Al/^{27}Al$ Ratio	From AMS: $^{26}Al/^{27}Al$ Ratio Uncertainty	
BLK	674	160448	5/14/21	9.834E-16	3.720E-16	Batch 3
BLKX	674	160453	5/14/21	1.009E-15	3.824E-16	
BLKXX	674	160454	5/14/21	5.103E-16	2.553E-16	
BLKXXX	674	160459	5/14/21	1.220E-15	4.074E-16	
BLK	669	160437	5/14/21	3.327E-16	3.186E-16	Batch 2
BLKX	669	160440	5/14/21	7.316E-16	3.275E-16	
BLKXX	669	160443	5/14/21	5.942E-16	2.659E-16	
BLKXXX	669	160446	5/14/21	9.320E-16	3.525E-16	
BLK	662	160426	5/14/21	7.947E-16	4.279E-16	Batch 1
BLKX	662	160433	5/14/21	8.046E-16	3.782E-16	
			AVERAGE	7.91E-16		
			STDEV	2.62E-16		

Table S4. ^{26}Al blank values. Blanks were processed in three batches (shown on the right).

Sample Name	Age (ka)	Decay-Corrected ^{10}Be Concentration (atoms g^{-1})	Decay-Corrected ^{10}Be Concentration 1σ Uncertainty (atoms g^{-1})	Decay-Corrected ^{26}Al Concentration (atoms g^{-1})	Decay-Corrected ^{26}Al Concentration 1σ Uncertainty (atoms g^{-1})	Decay-Corrected ^{26}Al/^{10}Be	Decay-Corrected ^{26}Al/^{10}Be 1σ Uncertainty
EB0	14	2.28E+04	2.72E+03	1.21E+05	1.29E+04	5.30	0.85
EH1	16.8	9.56E+03	1.54E+03	5.21E+04	6.76E+03	5.45	1.13
EB1	20.4	2.07E+04	1.91E+03	1.05E+05	1.22E+04	5.07	0.75
EH2	24	1.03E+04	1.23E+03	3.99E+04	8.46E+03	3.87	0.94
EB2	27.5	2.86E+04	2.43E+03	1.65E+05	1.49E+04	5.78	0.72
EH3	31	3.50E+04	3.15E+03	2.03E+05	1.81E+04	5.80	0.73
EB3	34.5	4.44E+04	1.33E+03	2.29E+05	1.57E+04	5.15	0.39
EH4	38	1.47E+04	1.05E+03	7.29E+04	7.19E+03	4.96	0.61
EB4	41.5	4.43E+04	1.51E+03	1.90E+05	9.45E+03	4.28	0.26
EH5	45	1.38E+04	1.50E+03	8.13E+04	9.36E+03	5.89	0.93
EB5	52.5	2.96E+04	3.77E+03	1.53E+05	1.43E+04	5.16	0.82
EH6	60	3.37E+04	2.93E+03	1.96E+05	1.69E+04	5.82	0.71
EB6	65	3.73E+04	2.49E+03	2.19E+05	1.90E+04	5.89	0.64
WB0	14	7.18E+03	1.77E+03	3.49E+04	1.01E+04	4.86	1.85
WH1	16.8	6.72E+03	1.39E+03	2.26E+04	4.92E+03	3.36	1.01
WB1	20.4	7.63E+03	1.19E+03	3.87E+04	5.84E+03	5.07	1.10
WH2	24	7.51E+03	1.71E+03	3.96E+04	6.71E+03	5.28	1.50
WB2	27.5	1.21E+04	2.40E+03	5.19E+04	9.27E+03	4.30	1.15
WH3	31	1.09E+04	1.76E+03	5.34E+04	8.97E+03	4.91	1.15
WB3	34.5	1.36E+04	1.92E+03	5.22E+04	9.02E+03	3.83	0.85
WH4	38	1.10E+04	1.00E+03	6.40E+04	7.26E+03	5.82	0.85
WB4	41.5	1.57E+04	2.72E+03	8.00E+04	1.09E+04	5.09	1.12
WH5	45	1.28E+04	1.06E+03	6.65E+04	5.11E+03	5.20	0.59
WB5	52.5	1.99E+04	2.72E+03	9.66E+04	1.25E+04	4.85	0.91
WH6	60	1.60E+04	1.49E+03	5.74E+04	7.74E+03	3.59	0.59
WB6	65	1.62E+04	1.67E+03	6.00E+04	6.72E+03	3.70	0.56

Table S5. Decay-corrected ^{26}Al and ^{10}Be concentrations and ratios in North Atlantic ice-rafted debris. Measured ^{10}Be concentrations (from Table S1) and ^{26}Al concentrations (from Table S3) are shown here corrected for radioactive decay on the seafloor to the time of deposition.

Supplemental Materials References

Andrews, J.T., and Tedesco, K., 1992, Detrital carbonate-rich sediments, northwestern Labrador Sea: implications for ice-sheet dynamics and iceberg rafting (Heinrich) events in the North Atlantic: Geology, v. 20, p. 1087–1090, doi:10.1130/0091-7613(1992)020<1087:DCRSNL>2.3.CO;2.

Balco, G., Stone, J.O., Lifton, N.A., and Dunai, T.J., 2008, A complete and easily accessible means of calculating surface exposure ages or erosion rates from 10Be and 26Al measurements: Quaternary Geochronology, v. 3, p. 174–195, doi:10.1016/j.quageo.2007.12.001.

Bond, G. et al., 1992, Evidence for massive discharges of icebergs into the North Atlantic ocean during the last glacial period: Nature, v. 360, p. 245–249.

Broecker, W., Bond, G., Klas, M., Clark, E., and McManus, J., 1992, Origin of the northern Atlantic's Heinrich events: Climate Dynamics, v. 6, p. 265–273, doi:10.1007/BF00193540.

Channell, J.E.T., and Hodell, D.A., 2013, Magnetic signatures of Heinrich-like detrital layers in the Quaternary of the North Atlantic: Earth and Planetary Science Letters, v. 369–370, p. 260–270, doi:10.1016/j.epsl.2013.03.034.

Channell, J.E.T., Hodell, D.A., Romero, O., Hillaire-Marcel, C., de Vernal, A., Stoner, J.S., Mazaud, A., and Röhl, U., 2012, A 750-kyr detrital-layer stratigraphy for the North Atlantic (IODP Sites U1302-U1303, Orphan Knoll, Labrador Sea): Earth and Planetary Science Letters, v. 317–318, p. 218–230, doi:10.1016/j.epsl.2011.11.029.

Corbett, L.B., Bierman, P.R., Rood, D.H., Caffee, M.W., Lifton, N.A., and Woodruff, T.E., 2017, Cosmogenic 26Al/10Be surface production ratio in Greenland: Geophysical Research Letters, v. 44, p. 1350–1359, doi:10.1002/2016GL071276.

Downing, G.E., and Hemming, S.R., 2012, Late glacial and deglacial history of ice rafting in the Labrador Sea: A perspective from radiogenic isotopes in marine sediments: Geological Society Special Paper 487, p. 113–124.

Downing, G.E., Hemming, S.R., Jost, A., and Roy, M., 2013, 40Ar/39Ar hornblende provenance clues about Heinrich event 3 (H3): Geological Society Special Publication, v. 378, p. 245–263, doi:10.1144/SP378.18.

Gwiazda, R.H., Hemming, S.R., Broecker, W.S., Onsttot, T., and Mueller, C., 1996a, Evidence from 40Ar/39Ar ages for a Churchill province source of ice-rafted amphiboles in Heinrich layer 2: Journal of Glaciology, v. 42, p. 440–446, doi:10.1017/S0022143000003427.

Gwiazda, R.H., Hemming, S.R., and Broecker, W.S., 1996b, Provenance of icebergs during Heinrich Event 3 and the contrast to their sources during other Heinrich episodes: Paleoceanography, v. 11, p. 371–378, doi:10.1029/96PA01022.

Heisinger, B., Lal, D., Jull, A.J.T., Kubik, P., Ivy-Ochs, S., Knie, K., and Nolte, E., 2002, Production of selected cosmogenic radionuclides by muons: 2. Capture of negative muons: Earth and Planetary Science Letters, v. 200, p. 357–369, doi:10.1016/S0012-821X(02)00641-6.

Hemming, S.R., 2004, Heinrich events: Massive late Pleistocene detritus layers of the North Atlantic and their global climate imprint: Reviews of Geophysics, v. 42, doi:10.1029/2003RG000128.

Hemming, S.R., Bond, G.C., Broecker, W.S., Sharp, W.D., and Klas-Mendelson, M., 2000, Evidence from 40Ar/39Ar ages of individual hornblende grains for varying Laurentide sources of iceberg discharges 22,000 to 10,500 yr B.P: Quaternary Research, v. 54, p. 372–383, doi:10.1006/qres.2000.2181.

Hemming, S.R., Broecker, W.S., Sharp, W.D., Bond, G.C., Gwiazda, R.H., McManus, J.F., Klas, M., and Hajdas, I., 1998, Provenance of Heinrich layers in core V28-82, northeastern Atlantic: 40Ar/39Ar ages of ice-rafted hornblende, Pb isotopes in feldspar grains, and Nd-Sr-Pb isotopes in the fine sediment fraction: Earth and Planetary Science Letters, v. 164, p. 317–333, doi:10.1016/S0012-821X(98)00224-6.

Hemming, S.R., and Hajdas, I., 2003, Ice-rafted detritus evidence from 40Ar/39Ar ages of individual hornblende grains for evolution of the eastern margin of the Laurentide ice sheet since 43 14C ky: Quaternary International, v. 99–100, p. 29–43, doi:10.1016/S1040-6182(02)00110-6.

Hillaire-Marcel, C., de Vernal, A., Bilodeau, G., and Wu, G., 1994, Isotope stratigraphy, sedimentation rates, deep circulation, and carbonate events in the Labrador Sea during the last ~200 ka: Canadian Journal of Earth Sciences, v. 31, p. 63–89, doi:10.1139/e94-007.

Hodell, D.A. et al., 2017, Anatomy of Heinrich Layer 1 and its role in the last deglaciation: Paleoceanography, v. 32, p. 284–303, doi:10.1002/2016PA003028.

Hodell, D.A., Channeil, J.E.T., Curtis, J.H., Romero, O.E., and Röhl, U., 2008, Onset of "Hudson Strait" Heinrich events in the eastern North Atlantic at the end of the middle Pleistocene transition (~640 ka)? Paleoceanography, v. 23, p. PA4218:1-16, doi:10.1029/2008PA001591.

Hoffman, P.F., 1988, UNITED PLATES OF AMERICA , THE BIRTH OF A CRATON : Early Proterozoic Assembly and Growth of Laurentia: Annual Review of Earth and Planetary Sciences, v. 16, p. 543–603.

Lamy, F. et al., 2015, Glacial reduction and millennial-scale variations in Drake Passage throughflow: Proceedings of the National Academy of Sciences of the United States of America, v. 112, p. 13496–13501, doi:10.1073/pnas.1509203112.

Lien, Ø.F., Hjelstuen, B.O., Zhang, X., and Sejrup, H.P., 2022, Late Plio-Pleistocene evolution of the Eurasian Ice Sheets inferred from sediment input along the northeastern Atlantic continental margin: Quaternary Science Reviews, v. 282, p. 107433, doi:10.1016/j.quascirev.2022.107433.

Manighetti, B., McCave, I.N., Maslin, M., and Shackleton, N.J., 1995, Chronology for climate change: Developing age models for the Biogeochemical Ocean Flux Study cores: Paleoceanography, v. 10, p. 513–525, doi:10.1029/94PA03062.

Marcott, S.A. et al., 2011, Ice-shelf collapse from subsurface warming as a trigger for Heinrich events: Proceedings of the National Academy of Sciences of the United States of America, v. 108, p. 13415–13419, doi:10.1073/pnas.1104772108.

McCave, I.N., and Andrews, J.T., 2019, Distinguishing current effects in sediments delivered to the ocean by ice. I. Principles, methods and examples: Quaternary Science Reviews, v. 212, p. 92–107, doi:10.1016/j.quascirev.2019.03.031.

McKay, R. et al., 2022, A Comparison of Methods for Identifying and Quantifying Ice Rafted Debris on the Antarctic Margin: Paleoceanography and Paleoclimatology, v. 37, doi:10.1029/2021PA004404.

Naafs, B.D.A., Hefter, J., and Stein, R., 2013, Millennial-scale ice rafting events and Hudson Strait Heinrich(-like) Events during the late Pliocene and Pleistocene: A review: Quaternary Science Reviews, v. 80, p. 1–28, doi:10.1016/j.quascirev.2013.08.014.

Rasmussen, T.L., Oppo, D.W., Thomsen, E., and Lehman, S.J., 2003, Deep sea records from the southeast Labrador Sea: Ocean circulation changes and ice-rafting events during the last 160,000 years: Paleoceanography, v. 18, p. 1–15, doi:10.1029/2001pa000736.

Robinson, S.G., Maslin, M.A., and McCave, I.N., 1995, Magnetic susceptibility variations in Upper Pleistocene deep-sea sediments of the NE Atlantic: Implications for ice rafting and paleocirculation at the Last Glacial Maximum: Paleoceanography, v. 10, p. 221–250, doi:10.1029/94PA02683.

Rosell-Mele, A., Maslin, M.A., Maxwell, J.R., and Schaeffer, P., 1997, Biomarker evidence for “Heinrich” events: Geochimica et Cosmochimica Acta, v. 61, p. 1671–1678.

Snoeckx, H., Grousset, F., Revel, M., and Boelaert, A., 1999, European contribution of ice-rafted sand to Heinrich layers H3 and H4: Marine Geology, v. 158, p. 197–208, doi:10.1016/S0025-3227(98)00168-6.

Stoner, J.S., Channell, J.E.T., and Hillaire-Marcel, C., 1996, The magnetic signature of rapidly deposited detrital layers from the deep Labrador Sea: Relationship to North Atlantic Heinrich layers: Paleoceanography, v. 11, p. 309–325, doi:10.1029/96PA00583.